Human sperm swimming in a high viscosity mucus analogue

Kenta Ishimoto [a,b,c,*], Hermes Gadêlha [d,g], Eamonn A. Gaffney [a], David J. Smith [e,f,g], Jackson Kirkman-Brown [f,g]

[a] *Wolfson Centre for Mathematical Biology, Mathematical Institute, University of Oxford, Oxford OX2 6GG, UK*
[b] *The Hakubi Center for Advanced Research, Kyoto University, Kyoto 606-8501, Japan*
[c] *Research Institute for Mathematical Sciences, Kyoto University, Kyoto 606-8502, Japan*
[d] *Department of Mathematics, University of York, York YO10 5DD, UK*
[e] *School of Mathematics, University of Birmingham, Birmingham B15 2TT, UK*
[f] *Institute for Metabolism and Systems Research, College of Medical and Dental Sciences, University of Birmingham, Birmingham B15 2TT, UK*
[g] *Centre for Human Reproductive Science, Birmingham Women's and Children's NHS Foundation Trust, Birmingham B15 2TG, UK*

ABSTRACT

Remarkably, mammalian sperm maintain a substantive proportion of their progressive swimming speed within highly viscous fluids, including those of the female reproductive tract. Here, we analyse the digital microscopy of a human sperm swimming in a highly viscous, weakly elastic mucus analogue. We exploit principal component analysis to simplify its flagellar beat pattern, from which boundary element calculations are used to determine the time-dependent flow field around the sperm cell. The sperm flow field is further approximated in terms of regularised point forces, and estimates of the mechanical power consumption are determined, for comparison with analogous low viscosity media studies. This highlights extensive differences in the structure of the flows surrounding human sperm in different media, indicating how the cell-cell and cell-boundary hydrodynamic interactions significantly differ with the physical microenvironment. The regularised point force decomposition also provides cell-level information that may ultimately be incorporated into sperm population models. We further observe indications that the core feature in explaining the effectiveness of sperm swimming in high viscosity media is the loss of cell yawing, which is related with a greater density of regularised point force singularities along the axis of symmetry of the flagellar beat to represent the flow field. In turn this implicates a reduction of the wavelength of the distal beat pattern — and hence dynamical wavelength selection of the flagellar beat — as the dominant feature governing the effectiveness of sperm swimming in highly viscous media.

1. Introduction

Viewed in slow motion, the sperm flagellum reveals a graceful choreography, concealing the complex regulation of thousands of dynein molecular motors converting ATP into mechanical work and ultimately travelling waves of curvature along the flagellum (Brokaw, 1971; Lindemann and Leisch, 2010; Smith et al., 2009b). This movement, and its interaction with the surrounding fluid, induces local fluid flows (Dresdner and Katz, 1981), propels the cell forward (Gray and Hancock, 1955) and, most remarkably, the progressive velocity is relatively conserved even as the viscosity of the surrounding media increases by multiple orders of magnitude (Smith et al., 2009b).

Such resilience is poorly understood for sperm, but vital in navigating numerous highly viscous microenvironments en-route to the egg in the female reproductive tract (Suarez and Pacey, 2006). Nonetheless, one hypothesis for this resilience is that with increased resistance, whether viscous or structural, the flagellum curvature is less so that the hypothesized geometric clutching of dyneins is reduced, as detailed extensively by Lindemann (1996). In particular, more dyneins contract in a flagellum bend as it is of longer wavelength (Lindemann, 1996), at least in the proximal region of the flagellum (Smith et al., 2009b). This mechanism thus in turn suggests that there are more dynein contractions per unit time on average for a sperm swimming in a highly viscous medium and also, because the flagellum does slowdown at least a certain amount, there may be a greater force per contraction given the observed monotonic increase in contractile force with reduced dynein contraction velocity (Oiwa and Takahashi, 1988). However such concepts for the mechanisms that govern the remarkable abil-

ity of sperm to swim in highly viscous media, and their relative importance in the sperm response, remain at the level of hypothesis. As a consequence, there is extensive further scope for comparative studies of sperm in different rheologies, especially as viscosity extensively regulates sperm behaviour *in vivo* (Kirkman-Brown and Smith, 2011).

Similarly, differences in the fluid flows induced by sperm flagellar beating with changes in the surrounding medium are likely to inform our understanding of how the physical microenvironment influences the mechanical interaction of sperm with each other, obstacles, surfaces and even the egg. Such differences may also be important in appreciating how the local transport of signalling molecules changes with different rheologies (Dresdner and Katz, 1981). With the exception of a low-resolution study comparing the fluid flow induced by activated and hyperactivated hamster sperm (Dresdner and Katz, 1981), only the fluid flows surrounding an activated swimming human sperm cell in a low viscosity *in vitro* fertilization medium have been analysed in detail (Ishimoto et al., 2017). This study revealed a remarkably simple approximation to the fluid flow structure. In particular, in the reference frame of the swimming cell an oscillatory flow was induced, approximately corresponding to two triplets of regularised forces offset to either side of the flagellum turning on and off in a manner corresponding to a principal and reverse wave propagating down the flagellum. This prospectively allows simple, verified, analytical expressions to be used to represent the flow fields associated with sperm swimming. As a first consideration, this would in turn enable the integration of single cell dynamics and sperm-sperm interactions in population models of sperm, as well as motivating analogous studies for the flows induced by sperm and other microswimmers, in fluid media with different rheologies.

Hence, in this paper we will firstly recapitulate the digital capture of the flagellum waveform for a human sperm swimming in a dilute solution of methylcellulose, which has a viscosity of about 150 times that of water and *in vitro* fertilization media (Smith et al., 2009b). Following a standard principal component analysis (PCA) of the flagellar waveform to reduce its kinematics to a low dimensional expansion of PCA modes (Ma et al., 2014; Werner et al., 2014), as detailed in Section 2, we will use boundary element computational fluid dynamics (Pozrikidis, 1992) to determine the surrounding flow field.

We will proceed to also reduce the fluid flow to a low dimensional expansion of PCA modes, which can be subsequently approximated by the flow fields associated with a small number of regularised point force solutions (Ishimoto et al., 2017). Further analyses are performed to document mechanical measures, such as the rate of viscous dissipation. In turn, these mechanical measures and their associated flow fields will be compared to those emerging from human sperm swimming in low viscosity *in vitro* fertilization media, to further document and describe how sperm swimming and its associated mechanics is altered with a substantive increase in the viscosity of the surrounding media.

Finally, we will also discuss our comparative observations in the context of potential mechanisms governing the quite remarkable observation that progressive sperm swimming speeds are roughly maintained despite multiple order of magnitude increases in the surrounding fluid viscosity.

2. Methods

2.1. Flagellar waveform

2.1.1. Image acquisition

Further details of the experimental method may be found in Smith et al. (2009b). To summarise, human samples were collected from a normozoospermic research donor and sperm with the highest progressive motility, sufficient to penetrate approximately 2 cm into a capillary tube on the timescales of the experiment, were imaged in detail. This imaging took place approximately 10–20 μm from the capillary tube inside surface, using an Olympus (BX-50) microscope, together with a positive phase contrast lens ($20 \times /0.40 \infty/0.17$ Ph1 and depth of field $\sim 5.8\,\mu m$) and a Hamamatsu Photonics C9300 CCD camera.

In particular, the Smith et al. (2009b) study firstly reported that the characteristics of these analysed cells differed extensively for different penetration media. In addition the study observed that with a fixed penetration medium, the sperm flagellum beat and swimming behaviour of these highly motile sperm were well-represented by an individual cell. Thus, analogously, we analyse a representative individual sperm, whose swimming and flagellum beat was captured in the above study as part of observations for 19 cells swimming within a sperm penetration medium based on supplemented Earle's Balanced Salt Solution and an addition of 1% methylcellulose. This is referred to as high viscosity medium (HVM) below. These observations and subsequent analysis will also be contrasted with those for a representative individual sperm, whose swimming and flagellum beat was captured in the Smith et. al. study (Smith et al., 2009b) as part of observations for 16 cells swimming within a watery – low viscosity – medium (LVM).

Measurements of the high viscosity medium's properties were conducted with a Bohlin CVO120 HR cone-and-plate rheometer yielded a storage modulus of $G' = 0.76$ Pa and a shear modulus of $G'' = 4.16$ Pa at a frequency of $f = 5$ Hz, i.e. an angular frequency of $\omega = 2\pi f = 10\pi$ rad s^{-1}. Fitting with a linear Maxwell fluid model in turn revealed a fluid relaxation time of $\lambda = 0.006$ s and an effective viscosity of 0.14 Pa·s, with a small Deborah number of De$= 2\pi f\lambda = \omega\lambda = 0.19 \approx 0.2$ and thus the fluid exhibits a similar magnitude of viscosity compared to midcycle mucus, though with significantly less elasticity (Khan et al., 1977; Smith et al., 2009b).

The location of the flagellum in the microscope focal plane, as a function of arclength s, measured from the cell head, and time t was extracted from the imaging data via bespoke MATLAB ©software (Smith et al., 2009b). Hence the angle between the flagellum tangent and the sperm head, denoted $\psi(s, t)$ is readily extracted. These digitised waveforms, which are essentially planar, do not exhibit extensive curvature in the proximal region of the flagellum but possess a distal meander (Fig. 1a and b), and this dynamics is generally associated with the tapering accessory structures of the mammalian flagellum with increasing arclength (Fawcett, 1975; Gaffney et al., 2011; Lindemann, 1996).

2.1.2. Dimensional reduction of the flagellar waveform

As previously implemented for bull spermatozoa by Ma et al. (2014) and human spermatozoa in our previous study (Ishimoto et al., 2017), and reviewed in Werner et al. (2014), principal component analysis (PCA) is used to decompose the angle ψ for the data-set acquired by the digital capture of the human sperm flagellum waveform, as summarised in Fig. 1. In detail, with a uniform discretisation of the arclength $s_1, \ldots, s_m$, and time, $t_1, \ldots, t_n$, one can construct the $n \times m$ angle matrix $\psi_{i\alpha} = \psi(t_i, s_\alpha)$, its temporal average

$$\bar{\psi}_\alpha = \frac{1}{n}\sum_{p=1}^{n}\psi_{p\alpha}$$

for any $i \in \{1, \ldots, n\}$ and the covariance matrix,

$$S_{\alpha\beta} = \frac{1}{n}\sum_{i=1}^{n}(\psi_{i\alpha} - \bar{\psi}_\alpha)(\psi_{i\beta} - \bar{\psi}_\beta).$$

The eigenvectors of the latter $m \times m$ matrix provide an m-dimensional basis for the flagellar wave, which we order by the size of the associated eigenvalues $\lambda_1 \geq \ldots \geq \lambda_m$. Each eigenvector,
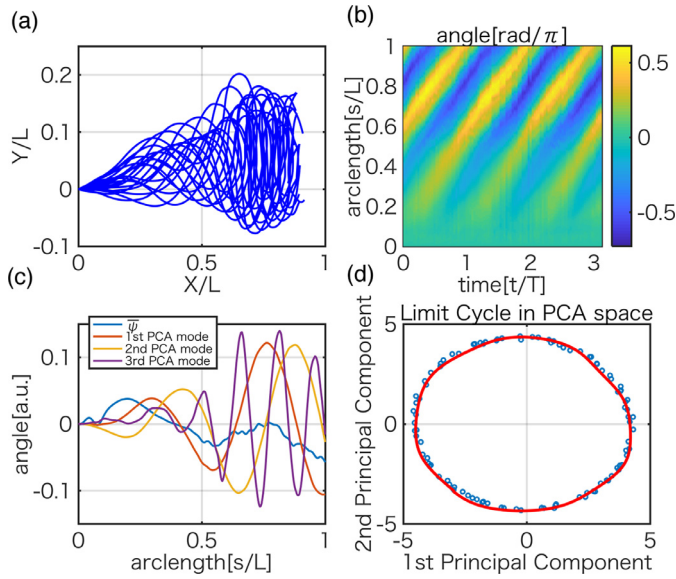
Fig. 1. The sperm flagellar waveform and its reconstruction, presented with the length and timescales nondimensionalised by the flagellar length, L, and the beat period time, T. (a) Superimposed snapshots of the digitally captured flagellar waveform with its head translated to the origin. (b) The flagellar tangent angle, $\psi(s, t)$. Note that approximately 10% of the distal flagellum data is lost during image capture. (c) The first three PCA modes of the flagellum angle, ψ, with $\bar{\psi}(s)$ denoting the temporal average of $\psi(s, t)$. (d) The trajectory of the first two PCA mode coefficients (blue), with the associated limit cycle orbit, in the phase space (red). (For interpretation of the references to colour in this figure legend, the reader is referred to the web version of this article.)

also known as a PCA mode, thus corresponds to a set of angles at the discretised values of s, and thus effectively a flagellum shape. The PCA decomposition then approximates the flagellum angles $\psi(s, t)$ as a time dependent weighted linear sum of these shapes. The first three eigenvectors, associated with eigenvalues $\lambda_1, \ldots, \lambda_3$, are plotted in Fig. 1c. In particular, truncating the PCA decomposition to include only the first two PCA modes nonetheless captures 96.9% of the cumulative variance, that is $(\lambda_1 + \lambda_2)/\text{trace}(S) = 0.969$, while truncating with only the first three modes captures 97.6%. Thus, respectively there is a 3.1% and 2.4% variation in the flagellar shape that is not accounted for on restricting the PCA mode decompositions. Hence using the first two or three PCA mode terms in the PCA decomposition leads to an extensive reduction and simplification of the data-set but yet with highly limited error.

The first p time-dependent coefficients of a PCA decomposition for a beating flagellum also define a trajectory in a p-dimensional phase space and for $p = 2$ with the current waveform, we find an approximately circular phase trajectory as plotted in Fig. 1d. Furthermore, by using a phase parameter to describe this time dependent trajectory, a phase space limit cycle can be determined, as given by the red curve in Fig. 1d (Kralemann et al., 2008; Ma et al., 2014). In particular, note that this limit cycle averages the dynamics over multiple flagellar beat patterns, and does not deviate extensively from individual data points. Hence fluctuations within a single flagellum beat of an individual cell are not large and the use of the limit cycle also reduces the impact of such fluctuations on the analysis pursued later.

It is also immediately apparent that these approximately circular limit-cycle trajectories contrast markedly with the dumbbell-like phase-trajectories and limit cycles associated with human sperm flagellar beating in a low viscosity *in vitro* fertilisation medium (see Ishimoto et al., 2017). A further difference between the low and high viscosity data for a human sperm is that the ad-
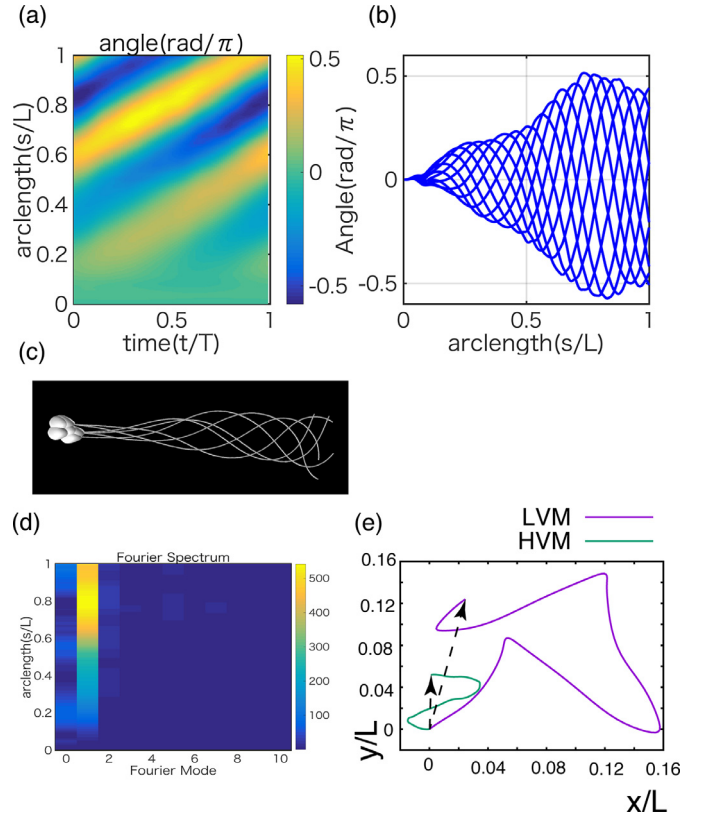

Fig. 2. The reconstructed approximation to the flagellar waveform as the limit cycle of the closed trajectories in the 2-dimensional flagellar shape PCA phase space. (a) The reconstructed flagellar tangent angle, $\psi_{rec}(s, t)$ during one beat cycle. The timescale and lengthscale are non-dimensionalised by the beat cycle period T and the flagellar length L. (b) Superimposed snapshots of the reconstructed flagellar tangent angle, non-dimensionalised as in (a). (c) Superimposed snapshots of the computational sperm with this waveform freely swimming during one beat cycle. (d) The Fourier spectrum for the reconstructed flagellar tangent angle, which emphasises a dominant frequency in the flagellum beat. (e) The swimming trajectory for the head-tail junction over one beat period of the virtual sperm, with the reconstructed flagellar waveform moving in the high-viscosity medium (HVM), is plotted in green, with coordinates provided in the Supporting Material. The associated net displacement during one beat cycle is shown via the dotted arrow. For comparison, the analogous trajectory for the low viscosity medium (LVM) is given in purple, together with the net displacement via the associated dotted arrow (Ishimoto et al., 2017). (For interpretation of the references to colour in this figure legend, the reader is referred to the web version of this article.)

dition of the third PCA mode in the high viscosity case does not lead to marked improvement in capturing the flagellum shape, due to the absence of extensive deformation in the proximal region of the flagellum. Hence the first two PCA modes are sufficient to capture the characteristic properties of the flagellar waveform. Hence, hereafter, we consider the flagellum beat associated with the $p = 2$ dimensional PCA phase plane trajectory of Fig. 1d and the corresponding angle, denoted $\psi_{rec}(s, t)$ is given as a heat map in Fig. 2a and via a plot of this angle as a function of arclength for numerous fixed snapshots of time in Fig. 2b. The latter highlights the curvature in the distal region of the flagellum due to the rapid angle changes in this region. The Fourier spectrum of $\psi_{rec}(s, t)$ with respect to the time is also displayed in Fig. 2d, which highlights a dominant first Fourier mode. This, together with the structure of Fig. 2a, emphasises that a dominant single temporal frequency propagates in a travelling wave along the flagellum.

2.2. Hydrodynamics of Stokes and linear Maxwell flow

As characterized by a very small Reynolds number, the fluid flow around a swimming sperm is essentially inertialess. Hence,

with $\boldsymbol{\sigma}$ denoting the stress tensor one has the momentum balance $\nabla \cdot \boldsymbol{\sigma} = \mathbf{0}$, which is supplemented by incompressibility $\nabla \cdot \boldsymbol{u} = 0$ for the velocity field $\boldsymbol{u}$. We also have no-slip conditions on the sperm and the glass surface, estimated to be roughly 15 microns below the swimming sperm (Ishimoto et al., 2017; Smith et al., 2009b), together with suitable boundary conditions at spatial infinity. The latter conditions here are simply that of no-flow. To detail the boundary conditions, let the region external to the swimmer be denoted by $\Omega(t)$, with a time-dependent sperm cell boundary S, and let any fixed boundary surfaces be denoted by S_*. Thus

$$\boldsymbol{u}(\boldsymbol{x}, t) = \boldsymbol{u}_S(\boldsymbol{x}, t) \quad \text{for } \boldsymbol{x} \in S, \quad \boldsymbol{u} = \mathbf{0} \quad \text{for } \boldsymbol{x} \in S_*,$$
$$\text{and } \boldsymbol{u} \to \mathbf{0} \text{ as } |\boldsymbol{x}| \to \infty,$$

where $\boldsymbol{u}_S(\boldsymbol{x}, t)$ is the velocity at point $\boldsymbol{x}$ and time t on the surface of the sperm cell. In particular, this can be written in terms of the velocity, $\boldsymbol{U}$, and angular velocity $\boldsymbol{\Omega}$ of a cell fixed reference frame, without loss defined by an origin at the head-flagellum junction and axes fixed in the cell body, together with the known, arclength and time dependent, velocity of the flagellum relative to this cell fixed frame. A constitutive relation is required to close these equations. For a Newtonian fluid, the stress tensor is given by

$$\sigma_{ij} = -p\delta_{ij} + \tau_{ij}, \quad i, j \in \{1, 2, 3\},$$

for a pressure field p, the Kronkecker delta δ_{ij}, and a deviatoric stress tensor

$$\boldsymbol{\tau} = 2\mu \boldsymbol{D}, \quad \text{where} \quad D_{ij} = \frac{1}{2}\left(\frac{\partial u_i}{\partial x_j} + \frac{\partial u_j}{\partial x_i}\right)$$

with μ the constant viscosity of the fluid. In contrast for a linear Maxwell fluid the deviatoric stress tensor is instead given by

$$\lambda\frac{\partial \boldsymbol{\tau}}{\partial t} + \boldsymbol{\tau} = 2\mu \boldsymbol{D},$$

where λ is the elastic relaxation time. The presence of a time derivative entails that the memory-less property of Stokes flow is not inherited by the dynamics of a linear Maxwell fluid and thus one must also give initial conditions. For definiteness we assume that sufficiently in the past, at $t \leq t_0$, the sperm and flow are stationary and the pressure constant, without loss zero, though the impact of the initial conditions decays on a timescale of λ, so that once $t - t_0 \gg \lambda$ the impact of the initial conditions is negligible.

2.3. The computational virtual sperm

In the Appendix we firstly demonstrate that, in the absence of inertia, predictions for the velocity and trajectories of the sperm cell are unchanged between linear Maxwell and Newtonian fluids. Thus, given the high viscosity medium is characterised by a linear Maxwell fluid with De ≈ 0.2, boundary element methods can be used to calculate the linear and angular velocities of the cell, together with its trajectory and surrounding flow field given the flagellar waveform of Fig. 2 (Ishimoto and Gaffney, 2014; 2016; 2017).

However, boundary element methods cannot be used analogously to exactly determine the mechanical power consumption (Ishimoto and Gaffney, 2016) for sperm swimming in HVM. The exact expression is given by

$$P = \int_S \boldsymbol{f}_{hyd}(\boldsymbol{x}') \cdot \boldsymbol{u}(\boldsymbol{x}') \, dS_{\boldsymbol{x}'}, \tag{1}$$

where $\boldsymbol{f}_{hyd}$ is the surface traction on the cell surface S and its exact determination by boundary element methods is limited to Newtonian media. Nonetheless, as demonstrated in the Appendix via scaling relationships, using Newtonian theory as a proxy for linear Maxwell theory results in estimates for the power, P, that are accurate to a relative error of about 100De% $\approx 20\%$, which is sufficient for our purposes.

Fig. 3. The tapering flagellum used for the power calculations, where in contrast to velocity field and trajectory calculations, which are insensitive to such details, the flagellum profile has a non-trivial, but modest, influence on the modelling predictions.

The computational human spermatozoon has a prolate ellipsoidal head which is deformed to generate a typical human sperm cell body shape, with analytical expressions for the shape of the sperm head given in previous studies (Ishimoto and Gaffney, 2014; 2016). For many simulations, the cell body is connected to a cylindrical flagellum of length $L = 56$ μm (e.g. Smith et al., 2009a) and diameter $d = 250$ nm, as shown in Fig. 2c. The latter is clearly an underestimate in the proximal region of the mammalian sperm flagellum, where the diameter is about 1 μm (e.g. Fig. 5 in Woolley, 2003) and an overestimate in the distal region where the mammalian flagellum loses its accessory structures (Fawcett, 1975; Lindemann and Mitchell, 2007). However, previous studies show that there is essentially no difference in modelling predictions of velocities with the boundary element method and a prescribed waveform for flagellar diameters in the range of 0.1–1 μm, e.g. Fig. 4 of Ishimoto and Gaffney (2014). This is also observed here for the predicted fluid flows and therefore the simpler, cylindrical, flagellum is used for flow calculations below. However, for power calculations the flagellum profile can have a modest but non-trivial impact and hence for such calculations below we work specifically with a tapering flagellum, as depicted in Fig. 3, where the most proximal flagellum diameter is 1 μm.

3. Results

3.1. Time-averaged flow field

For simplicity, the fluid velocity field relative to the sperm head-tail junction is determined via BEM in the absence of external boundaries. The magnitude of the resulting time-averaged velocity field is presented in the flagellar beat plane (defined as the xy plane), and in a plane perpendicular to the beat plane (defined as the yz plane) in Fig. 4 via the colourbar, with the projected streamlines in white. Since the swimmer is force-free, the magnitude of the velocity field associated with sperm swimming scales with r^{-2} in the far-field (Figure not shown), where r is the distance from the head-flagellum junction. Hence the multipole expansion for the far flow field is not proportional to a Stokeslet but instead a Stokeslet-dipole, $\lambda \mathbf{G}^d$, where $\mathbf{G}^d$ is a Stokeslet-dipole, oriented such that the forces lie on the time-averaged symmetry axis and push fluid away from the cell along this axis. Thus when $\lambda > 0$ (Smith and Blake, 2009) the one can observe fluid moving away from the cell along its long axis and the sperm is a *pusher* swimmer; the converse with $\lambda < 0$ is defined as a *puller* swimmer. Unsurprisingly, one can infer the time-averaged swimming of the sperm corresponds to a pusher, by inspection of Fig. 2, as also observed for sperm swimming in a low viscosity *in vitro* fertilisation medium (Ishimoto et al., 2017).

3.2. Coarse-graining the flow field

3.2.1. Dimensional reduction of the time-dependent flow field

The time dependent flow field surrounding the sperm has been calculated using the reconstructed flagellar waveform, and is presented in a reference frame co-moving with the sperm as a movie in the Supporting Material. Its complexity is illustrated by the
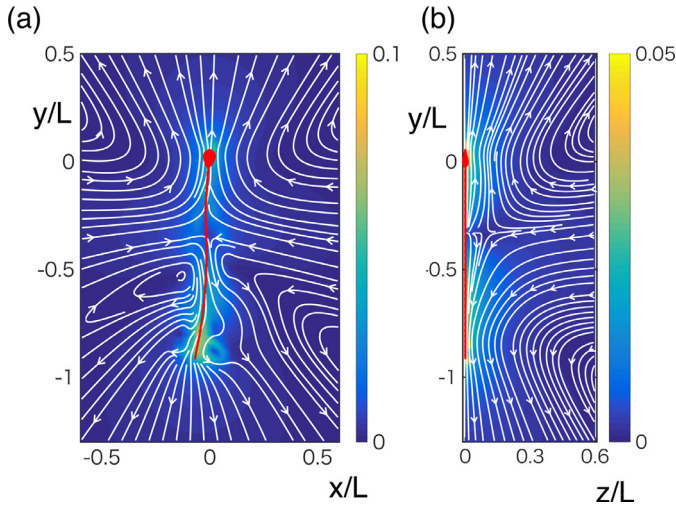
(a) (b)

Fig. 4. The time-averaged fluid flow around a human sperm swimming in high viscosity medium (HVM), relative to the sperm head-tail junction. The velocity magnitude is given in units of L/T via the colourbar. (a) The time-averaged flow field magnitude is given by the colourbar and the projections of the streamlines in the beating plane of the flagellum, which is defined as the xy plane, are given in white. (b) The analogous plot for the time-averaged flow field in the plane perpendicular to the beating plane, defined as the yz plane.

changes in the direction of the flow ahead of the sperm and hence we apply PCA to the fluid flow field to simplify its structure, without an extensive loss of accuracy or information. Consider a uniform discretisation of time, $t_1, \ldots, t_n$ and let m denote the number of mesh points in a spatial discretisation of the physical domain, with $\alpha \in \{1 \ldots 3m\}$ indexing the set $(e_{q_1(\alpha)}, x_{q_2(\alpha)})$. Here, respectively, $q_1(\alpha) \in \{1, 2, 3\}$ is the axis associated with α, and $q_2(\alpha) \in \{1, \ldots, m\}$ is the mesh point associated with α. Defining $u_{i\alpha} = e_{q_1(\alpha)} \cdot u(t_i, x_{q_2(\alpha)})$, and the velocity field time average

$$\bar{u}_\alpha = \frac{1}{n} \sum_{p=1}^{n} u_{p\alpha}, \qquad i \in \{1 \ldots n\},$$

one can construct the covariance matrix

$$S_{\alpha\beta}^{vel} = \frac{1}{n} \sum_{i=1}^{n} (u_{i\alpha} - \bar{u}_\alpha)(u_{i\beta} - \bar{u}_\beta),$$

of dimension $3m \times 3m$, thus allowing the implementation of PCA. Hence, we have a collection of spatially homogeneous, temporally constant velocity fields for the PCA modes, the first five of which are plotted in Fig. 5. Furthermore, the PCA expansion for the velocity field is simply a weighted sum of such PCA modes, with time dependent coefficients, and the cumulative variances for the first n terms, denoted c_n, are given by $c_1 = 0.628$, $c_2 = 0.901$, $c_3 = 0.935$, $c_4 = 0.956$, $c_5 = 0.969$. Hence, even just an expansion with first two modes captures more than 90% of the variation in the flow field.

3.2.2. Regularised Stokeslet decomposition

Following our previous study Ishimoto et al. (2017), we approximate the steady PCA modes with regularised Stokeslets (Cortez, 2001), which are more convenient than point singularities as they allow the representation of forces that manifest over different lengthscales without large numbers of singularities. We proceed by expanding the velocity field of PCA mode s, denoted $\tilde{u}^s(x)$, via

$$\tilde{u}^s(x) = \sum_{k=1}^{K_s} f^{(s,k)} \cdot G_{\epsilon^{(s,k)}}(x, x_0^{(s,k)}),$$

where

$$G_\epsilon = \frac{(r^2 + 2\epsilon^2)I + rr}{(r^2 + \epsilon^2)^{3/2}}$$

is a regularised Stokeslet (Cortez, 2001), with $r = x - x_0^{(s,k)}$, $r = |r|$, and I denotes the identity tensor. Least squares fitting is used to determine the position of each singularity $x^{(s,k)}$ together with the associated magnitude $f^{(s,k)}$ and regularization parameter $\epsilon^{(s,k)}$, with the latter representing the lengthscale over which each force contribution acts in the regularised Stokeslet decomposition. The number of singularities in the summation, K_s, is determined by the minimal number that yield a reasonable fit for each flow PCA mode, in this case $K_1 = 3$, $K_2 = 4$ for the lowest 2 modes and the resulting coefficients for this decomposition of PCA modes are detailed in the Supporting Material.

To generate an approximation of the velocity field using regularised singularities, we project the $3m$ dimensional vector $u_{i\alpha}$ of the original velocity field onto the span of the velocity vectors $\tilde{u}_\alpha^s = e_{q_1(\alpha)} \cdot \tilde{u}^s(x_{q_2(\alpha)})$, $s \in \{1, \ldots, Q\}$ for each time point $i \in \{1, \ldots, n\}$. The resulting projection at timepoint i is thus a weighted linear summation of the $\tilde{u}_\alpha^s$, and hence also a weighted linear summation of regularised Stokeslets. For the latter summation the coefficients in general vary with the timepoint i but are the same for each collection of regularised Stokeslets approximating a given PCA mode.

This approximation to the original velocity field at timepoint i, at meshpoint $q_2(\alpha)$ and in the direction $q_1(\alpha)$ is denoted $u_{i\alpha}^{*Q}$ and can be used to construct the $3m \times 3m$ covariance matrix

$$S_{\alpha\beta}^{*Q} = \frac{1}{n} \sum_{i=1}^{n} (u_{i\alpha}^{*Q} - \bar{u}_\alpha^{*Q})(u_{i\beta}^{*Q} - \bar{u}_\beta^{*Q}), \qquad (2)$$

with the temporal average $\bar{u}_\alpha^{*Q}$ defined analogously to the average of the observed velocity field. Then the ratio trace $(S^{*Q})/\text{trace}(S^{vel})$ is a measure of the proportion of the variance in the original flow that is captured by regularised Stokeslet approximation of the Q-level PCA mode expansion. In turn, the cumulative contribution rate for the regularised Stokeslet approximation to the $Q = 2$ PCA expansion is 0.878, which is very close to the cumulative variance of the $Q = 2$ PCA decomposition, namely $c_2 = 0.901$.

Therefore, the lowest two flow PCA modes are each well approximated by a regularised forces, with no net force acting on the sperm with three and four lateral forces along the flagellum, corresponding to $K_1 = 3$, $K_2 = 4$, as summarized in Fig. 6a. Focusing on the forces active along the flagellum, the two modes of lateral forces in the high viscosity medium are oscillatory and out of phase with respect to arclength variation, as observed in Fig. 6a. Their respective time-dependent coefficients are given in the Supporting Information and exhibit both an oscillation and a phase-lag, as seen in the phase plane trajectory of Fig. 6b and the plot of coefficients with time in Fig. 6c. In addition the arclength and temporal phase lags are such that these two standing waves combine to give a travelling wave along the flagellum to good approximation.

For instance, mode 2 has a time-dependence in phase with $\sin(\omega t)$ from Fig. 6c, while mode 1 is approximately in phase with $-\cos(\omega t)$. Noting that y in this plot decreases along the flagellum, the spatial dependence of the mode 2 contribution is in phase with $\sin(k(y + \xi))$, with $\xi \sim 0.55$, while mode 1 has a spatial dependence in phase with $-\cos(k(y + \xi))$. This may be as inferred by noting that mode 2 is of zero magnitude at $y = -\xi$, and increasing as y decreases from $y = -\xi$, while mode 1 is of peak negative amplitude at $y = -\xi$. There is clearly also an arclength modulation of the wave amplitude, summarised by the function $A(y)$, and so we
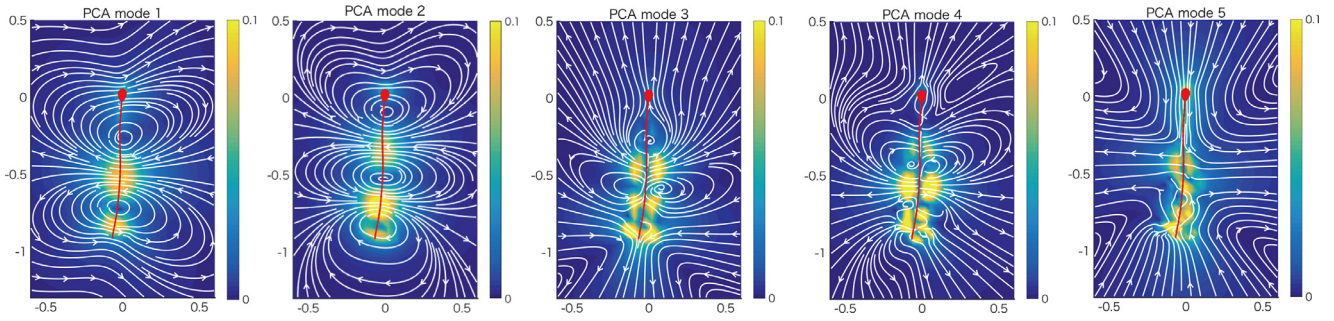
Fig. 5. The first five PCA modes of the time-dependent fluid velocity field. With the same units of L/T for velocity used in Fig. 4, the velocity magnitude of the flow projected on the flagellum beat plane, the xy plane, is given by the colourbar, with the projection of the streamlines onto the beat plane given in white.

have that the sum of the two standing waves is approximately

$$A(y)[\cos(\omega t)\cos(k(y+\xi)) - \sin(\omega t)\sin(k(y+\xi))]$$
$$= A(y)\cos(k(y+\xi) + \omega t),$$

which is an amplitude-modulated travelling wave in the negative y-direction, towards the distal flagellum. Associated with this wave are the corresponding lateral forces on the sperm cell body, as given by the regularised stokeslets near $y=0$ in Fig. 6a.

A further, perhaps counter-intuitive, feature of high viscosity swimming is that the majority of the forces in the regularised Stokeslet expansion are predominantly lateral. In particular, the proportion of the forces along the axis of symmetry of the sperm cell are small in comparison to a sperm swimming in a low viscosity, *in vitro* fertilization, medium as may be inferred by comparing Fig. 6a, with Fig. 6d, with the latter taken from Ishimoto et al. (2017). Hence even though the forces along the flagellum ultimately are responsible for progressive motility, they are subdominant within the local forces exerted the sperm flagellum in high viscosity media. A final contrast with the low viscosity results is that in high viscosity swimming, the coefficient for the leading order Stokeslet-dipole in the far-field multipole expansion is always positive throughout the beat cycle in a high viscosity medium. This is pusher swimming, in contrast to low viscosity human sperm motility, where the cell periodically behaves like a puller, even though its beat period averaged behaviour is that of a pusher (Ishimoto et al., 2017).

3.3. Swimming velocity, power and efficacy

We use the limit cycle reduction of the digitally captured flagellar wave in a high viscosity medium (see Fig. 2c). Denoting the time-average during one beat period as a bracket, $\langle\,\rangle$, the progressive swimming velocity and hydrodynamic power consumption are respectively given by

$$|\langle \mathbf{V}^{HVM}\rangle| = 5.1 \times 10^{-2}\frac{L}{T^{HVM}}, \qquad \langle P^{HVM}\rangle = 3.1 \times 10^{-2}\frac{\mu^{HVM}L^3}{(T^{HVM})^2},$$

where $\mathbf{V}$ is the swimming velocity, L is the flagellum length, T the beat period and μ the viscosity with the label HVM referring to high viscosity media. These values can be contrasted with the values for the human sperm in a watery low viscous medium (Ishimoto et al., 2017), for which we have

$$|\langle \mathbf{V}^{LVM}\rangle| = 1.2 \times 10^{-1}\frac{L}{T^{LVM}}, \qquad \langle P^{LVM}\rangle = 2.3 \times 10^{-2}\frac{\mu^{LVM}L^3}{(T^{LVM})^2},$$

where the label LVM refers to low viscosity media.

Note that the viscosity scales by a factor of about 155 between the high and low viscosity media and the beat period is 2.3 times as long in the high viscosity medium (Smith et al., 2009b). Hence we have the ratio of average dimensional velocities and powers are

given by

$$\frac{|\langle \mathbf{V}^{HVM}\rangle|}{|\langle \mathbf{V}^{LVM}\rangle|} \approx \frac{T^{LVM}}{T^{HVM}}\frac{5.1 \times 10^{-2}}{1.2 \times 10^{-1}} = 0.18,$$

$$\frac{\langle P^{HVM}\rangle}{\langle P^{LVM}\rangle} \approx \left(\frac{T^{LVM}}{T^{HVM}}\right)^2 \frac{\mu^{HVM}}{\mu^{LVM}}\frac{9.89 \times 10^{-5}}{1.1 \times 10^{-3}} = 3.9.$$

Note that despite an increase in viscosity of over 150 times, the progressive velocity reduces only by a factor of ≈ 5, with an increase in the power output of only a factor of ≈ 4.

Further note that the ratio of progressive velocities is strongly influenced by the fact that in low viscosity, there is extensive sperm cell yawing as reported in Smith et al. (2009b) and Ishimoto et al. (2017), and also shown in Fig. 2e. In contrast, if velocity magnitudes are taken before averaging and comparison, which takes into account the lateral movements of the cell in low viscosity media due to cell yawing, the ratio of dimensional velocities is given by

$$\frac{\langle|\mathbf{V}^{HVM}|\rangle}{\langle|\mathbf{V}^{LVM}|\rangle} \approx 0.048.$$

In particular, this change in velocity is due to cell yawing in the low viscosity medium since $\langle|\mathbf{V}^{LVM}|\rangle \approx 3.8|\langle\mathbf{V}^{LVM}\rangle|$.

Swimming efficiency is regularly considered in theoretical studies, and is defined via the ratio of the power needed to push a sphere of the same volume as the cell to the mechanical power of the swimming motion at the same mean speed. It is thus proportional to the ratio of the square velocity to power (Shum et al., 2010). However, our focus does not concern mechanical energy usage relative to driving a sphere, which addresses the impact of morphology for instance, but rather a comparison of the progression distance of a sperm cell for each unit of mechanical energy for motility in low and high viscosity media. Given power is energy per unit time and velocity is distance per unit time, we thus require the ratio of velocity to power to access the distance travelled per unit of mechanical energy, which is equivalent to the reciprocal of the "cost of transport" used in allometric scaling studies (e.g. Bale et al., 2014). Hence we define efficacy as the progressive swimming speed per unit of power consumption for the swimming sperm explicitly by

$$\zeta = \frac{|\langle\mathbf{V}\rangle|}{\langle P\rangle}, \tag{3}$$

where the brackets denote beat cycle averaging and we explore how this efficacy changes between swimming in high and low viscosity media.

First we note that with $\mathbf{u}_f(s,\,t)$ denoting the flagellum velocity, as a function of flagellum arclength and time and relative to the reference frame fixed in the sperm cell body, the underlying equations and boundary conditions for the fluid flow exhibit the
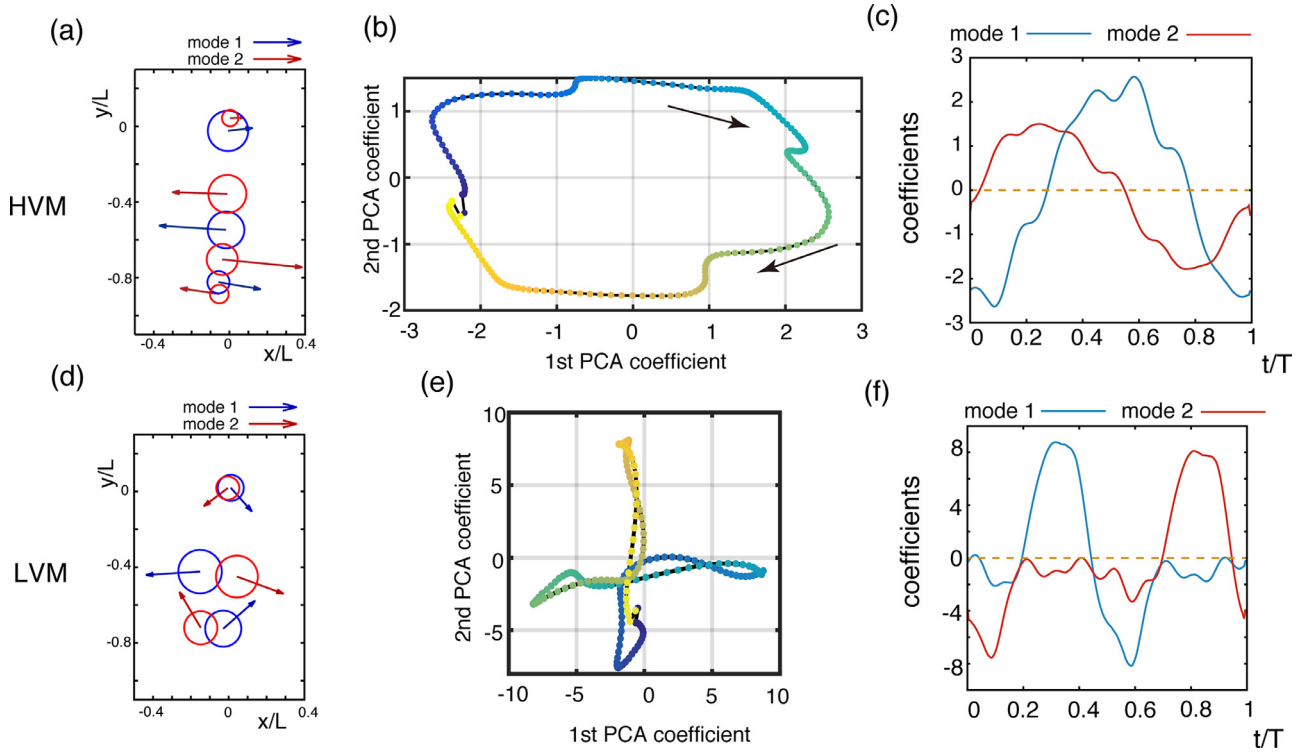
Fig. 6. (a) The regularised Stokeslet approximation for the first two PCA modes of the velocity field induced by sperm swimming in high viscosity medium. The origin, size and direction of the arrows give the location, magnitude and direction of the force singularities. The circle radius corresponds to the regularization parameter, ϵ. (b) The phase space of the first two PCA modes for the velocity field associated sperm swimming in the high viscosity medium, with the colour evolving with increasing time, from blue at early time to yellow. (c) A time plot of the coefficients for the first two PCA modes in the phase space trajectory depicted by (b) in terms of the non-dimensional time, t/T, where T is the beat period. (d)(e)(f) For comparison, the regularised Stokeslet approximation for the first two PCA modes of the velocity field due to a sperm swimming in a *low viscosity medium*, as determined by Ishimoto et al. (2017) are presented in (d) with the low viscosity analogues of (b)(c) given by (e),(f). Reproduction of (d)(e)(f) with permission from Ishimoto et al. (2017). (For interpretation of the references to colour in this figure legend, the reader is referred to the web version of this article.)

invariance

$$(\mu, p, \boldsymbol{u}, \boldsymbol{\sigma}, \boldsymbol{u}_f) \rightarrow (\Lambda\mu, \Lambda p, \boldsymbol{u}, \Lambda\boldsymbol{\sigma}, \boldsymbol{u}_f).$$

Hence, if the viscosity increases by a factor of Λ and the flagellum waveform is the same, then a solution of the sperm swimming problem is obtained with the same swimming speed and the power expenditure increased by a factor of Λ. Thus for fixed kinematics, that is a fixed flagellum waveform, and an increase in the viscosity by a factor of Λ we have the efficacy ζ reduces by factor of Λ and the viscosity-efficacy ratio

$$\eta := \frac{\mu^{HVM}\zeta^{HVM}}{\mu^{LVM}\zeta^{LVM}}$$

is unity.

Of course, the waveform does not remain unchanged with changes in viscosity. If on increasing the viscosity by a factor of Λ, the resulting changes of the flagellum result in an efficacy that is higher than the scaling result with fixed kinematics, then η will be greater than one. In other words, on comparing swimming in two viscosities differing by a factor of $\Lambda = \mu^{HVM}/\mu^{LVM}$, then a viscosity-efficacy ratio of $\eta > 1$ characterises a change in waveform that produces more progressive velocity per unit of mechanical power consumption in the higher viscosity medium relative to the $1/\Lambda$ reduction associated with keeping the waveform fixed.

Explicitly calculating η from the data we find

$$\eta = \frac{\mu^{HVM}}{\mu^{LVM}} \frac{|\langle \mathbf{V}^{HVM} \rangle|}{|\langle \mathbf{V}^{LVM} \rangle|} \frac{\langle P^{LVM} \rangle}{\langle P^{HVM} \rangle} \approx 155 \times 0.18 \times \frac{1}{3.9} \approx 7.2.$$

Hence, the change in the sperm flagellum waveform results in substantially greater efficacy in moving through a viscous fluid compared to swimming with the same waveform. A fundamental question is whether the data presented here can also suggest why the

waveform change might lead to this improvement of progressive velocity per unit power and we explore this further below.

In particular, the absence of cell-yawing in the high-viscosity medium does not appear to be sufficient to explain this observation in isolation, as taking the velocity magnitude before averaging yields a viscosity-efficacy ratio of

$$\frac{\mu^{HVM}}{\mu^{LVM}} \frac{\langle |\mathbf{V}^{HVM}| \rangle}{\langle |\mathbf{V}^{LVM}| \rangle} \frac{\langle P^{LVM} \rangle}{\langle P^{HVM} \rangle} \approx 155 \times 0.048 \times \frac{1}{3.9} \approx 2 > 1.$$

Consequently, a contribution to the above improvement observed in the efficacy associated with the flagellum waveform change is observed even when examining averaging only after taking the velocity magnitude and thus accounting for yaw. Hence, the loss of cell yawing cannot fully explain the relatively increased efficacy that accompanies the change in flagellar waveform for high viscosity swimming. Other factors thus contribute, such as the change in internal mechanics of the flagellum associated with the changed waveform. Nonetheless, these scales also indicate that the loss of cell yawing is the most important factor in the relative improvement of progressive swimming speed per unit of mechanical power imparted to the surrounding fluid with waveform change for a sperm, on comparing the mechanics of swimming in a low viscosity and a high viscosity medium.

4. Discussions and conclusions

We have first of all examined the flow field generated by a sperm swimming in a high-viscosity, weakly elastic, medium of dilute methylcellulose. Using techniques that have been previously reported (Ma et al., 2014; Werner et al., 2014) we used principal component analysis (PCA) to simplify the beating pattern of the

flagellum, via a limit cycle in the PCA phase space, and this simplified beat pattern was then used to determine the velocity field surrounding the sperm using boundary element method (BEM) calculations and this field was then also approximated in terms of velocity PCA modes (Ishimoto et al., 2017). This velocity field was further approximated using a small number of regularised Stokeslets and we confirmed that such approximations nonetheless capture most of the variance of the flow field.

Even a superficial inspection of the high viscosity flows compared to the low viscosity flow, for instance by comparing Fig. 6a, with Fig. 6b, confirms the many previous observations that the surrounding fluid is a major regulator of sperm behaviour (Brokaw, 1966; Kirkman-Brown and Smith, 2011; Rikmenspoel, 1984; Smith et al., 2009b). Considering this contrast in more detail, we have from previous studies (Ishimoto et al., 2017) that in low viscosity media, the overall impact of the sperm on the surrounding fluid is effectively blinking dynamics, associated with turning the PCA modes on and off in time, which gives rise to phase trajectories that are approximately cross-like with only one mode active at most timepoints during the beat cycle (Fig. 6e and f and Ishimoto et al., 2017). In contrast for the flows induced by high viscosity swimming we have, to a good approximation, a temporally phase-lagged sum of two spatially phase-lagged standing waves, which is equivalent to a travelling wave of forces propagating down the flagellum. Such differences far exceed the fluctuations observed in the data for an individual cell, as emphasised by the small differences between the phase plane points and the average limit cycle.

There are also further differences, for example in high viscosity media the sperm has always been observed to be a pusher, whilst sperm swimming in low viscosity media are pullers at certain points in the beat cycle. Finally, in high viscosity media the forces induced by sperm on the surrounding fluid are predominantly lateral only, in contrast to low viscosity swimming but the extent of cell yawing is greatly reduced in high viscosity media, with the latter observation reported in Kirkman-Brown and Smith (2011).

These observations emphasize that the mechanics of sperm interactions with their surrounding fluid, and the surrounding flow fields, are fundamentally altered with changes in rheology. Thus the hydrodynamic interactions of sperm with each other, obstacles and boundaries differ in high viscosity media, as is the means by which a sperm exerts its influence and experiences the influence of surrounding cells and boundaries via the surrounding flow field. Hence, for example, a physical understanding of sperm populations or sperm behaviours in confined geometries will fundamentally differ with the rheology of the surrounding media. While such observations have been made previously (Brokaw, 1966; Kirkman-Brown and Smith, 2011), the results presented here provide a means of quantifying and predicting the impact of such differences. For example, the regularised Stokeslet expansion may be used to upscale individual behaviours into population level models and thus provide a prospective means for predicting how population level sperm behaviour depends on rheology. In turn this will allow predictive modelling for the consideration of how sperm population behaviours are altered by their physical microenvironment. Furthermore, if such a predictive framework proves to be informative, it can increase our understanding of how population behaviours within the low viscosity media of standard clinical diagnostics and prospective sperm handling microdevices (Lopez-Garcia et al., 2008; Seo et al., 2007; Shao et al., 2007) translate to the *in vivo* setting.

Despite the increase in viscosity by two orders of magnitude, we observe that the progressive swimming velocity and mechanical power output of the flagellum in low and high viscosities are still within an order of magnitude between the media. Furthermore, the viscosity-efficacy ratio, η increases by a factor of about 7 on comparing high and low viscosity media. In turn, this indicates that the changes of the sperm flagellum waveform induce a greater efficacy, that is velocity per unit of mechanical power or distance per unit of mechanical energy, than would occur if the flagellum waveform was the same in the two media. Such observations are also consistent with prior modelling observations of improved mean sperm velocity per unit of mean mechanical power in high viscosity Newtonian media, deduced by simulating across a two-parameter family of waveforms constructed with cubic splines and adaptive knots to capture approximations of both low and high viscosity beat patterns (Wakeley, 2008).

In this study we proceeded to demonstrate that a factor of approximately 4 in the viscosity-efficacy ratio arises from the loss of yawing in the high viscosity medium. Thus, while there clearly is about a factor of two increase in the viscosity-efficacy ratio arising from the internal mechanics of the flagellum, as might ultimately be explained by changes in the numbers and rates of dynein contractions and the force-velocity curves of dynein contraction (Lindemann, 1996; Oiwa and Takahashi, 1988), the dominant contribution to the relative improvement in progression per unit of power appears to be the loss of yawing. This is despite the observation that the forces exerted by the flagellum on the fluid are predominantly lateral for the waveform in high viscosity. Instead, the loss of yaw might be anticipated by the high wavenumber of the distal flagellum beat in a more viscous medium, leading to a cancellation of lateral forces along the flagellum at any given instant, compared to low viscosity swimming where the flagellum is significantly less than two wavelengths. The changes in beat pattern wavelength can also be inferred from the increase in regularised Stokeslet density along the time-averaged symmetry axis of the cell, on comparing Fig. 6(b) with (a). However, one must recognise that conclusions drawn on such observations arise from comparing the observations of two sperm flagellum waveforms, albeit waveforms that are representative of the most highly motile human sperm in the respective low and high viscosity media, as reported previously (Smith et al., 2009b).

Subject to such caveats, this study therefore highlights that understanding the dominant mechanism governing the counter-intuitive effectiveness of progressive sperm swimming in very viscous media requires a focus on wavelength selection. In particular, one should consider the reduction of the wavelength associated with the distal waveform (Fig. 1a) in models of beat pattern formation and dynein regulation. In turn this suggests that flagellar self-organisation models incorporating motor-control mechanisms (Camalet and Jülicher, 2000; Hilfinger et al., 2009; Jülicher and Prost, 1997; Lindemann, 1994a; 1994b; Oriola et al., 2017; Riedel-Kruse et al., 2007) have the prospect of probing and predicting the conditions for when sperm do, and do not, yaw and thus when the dominant mechanism observed here for maintaining progression in high viscosity media given a limited power output will be present. While current models of flagellar beating may need refinement and further study to address such questions, one can nonetheless observe that increasing viscosity decreases the wavelength (e.g. Fig. 2d[inset] of Oriola et al., 2017), further indicating that the required waveform behaviour may emerge from relatively simple biophysics.

In summary, using PCA data reduction and boundary element methods we have highlighted that with an increase in viscosity by two orders of magnitude the human sperm flagellum induces a fluid flow that is well approximated by travelling wave of regularised points forces along the flagellum, in contrast to blinking, that is pulsing, force singularities in low viscosity media (Ishimoto et al., 2017). Such results are likely to find application in developing population level models of sperm dynamics that upscale individual level information. Furthermore, a consideration of efficacy for sperm swimming in high and low viscosity media emphasises that the loss of cell yawing is the dominant feature in explaining

how sperm can progress effectively with a limited power output despite very large increases in viscosity. In turn, this loss of yawing is anticipated to be due to the increase in the density of regularised forces along the time averaged symmetry axis of the cell in PCA approximations, thus indicating that understanding the dominant features of sperm progression at high viscosity might be reduced to a problem of wavelength selection in the complex self-organisation of the beating pattern in the mammalian flagellum.

Data Archiving

Acknowledgements

Appendix A. On the relation between Stokes flow and linear Maxwell theory

A1. Velocity fields and cell trajectories

The Newtonian momentum equations reduce to

$$-\frac{\partial p}{\partial x_i} + \mu \nabla^2 u_i = 0.$$

With p^M and u^M hereafter referring specifically to the linear Maxwell solution, one has that applying the operator $\mathcal{L} := (1 + \lambda \partial/\partial t)$ to the linear Maxwell fluid momentum equations gives

$$-\frac{\partial}{\partial x_i} \mathcal{L} p^M + \mu \nabla^2 u_i^M = 0$$

Hence setting

$$u_i^M = u_i, \quad p^M = \mathcal{L}^{-1} p,$$

solves the bulk equations and satisfies all boundary conditions. Given the sperm is also be imposed to be at rest for $t \leq t_0$ the above initial conditions are also satisfied, and the inverse operator $\mathcal{L}^{-1}$ is unique and we have a solution of the linear Maxwell problem with velocities identical to those of the Newtonian flow field problem. Since the velocity fields are predicted to be identical, so is the boundary velocity at all points on the rigid cell body and hence the cell body motion is identical, which fixes the predictions for the velocity and angular velocity of the cell fixed frame relative to the inertial frame, that is U and Ω, to be identical. Noting the flagellum motion relative to the cell fixed frame is identical by model construction, we have that the motion of the cell and thus its trajectory are identical. An alternative, more formal, proof of this result can also be found in recent work detailing the construction of a viscoelastic boundary element algorithm for microswimming (Ishimoto and Gaffney, 2017). However, the pressure differs between the linear Maxwell and Newtonian predictions and more generally so do the predictions of forces, stresses, power and efficacy.

A2. Power calculations

Noting that predicted velocities are indistinguishable, the mechanical power for the Newtonian and linear Maxwell theory are respectively given by

$$P = \int_S u_i \sigma_{ij} n_j dS, \quad P^M = \int_S u_i \sigma_{ij}^M n_j dS,$$

with n_j the jth component of the unit normal. Further, the Newtonian and linear Maxwell stress are related via

$$\sigma_{ij} = -p\delta_{ij} + 2\mu D_{ij} = -\mathcal{L} p^M \delta_{ij} + \mathcal{L} \tau_{ij}^M = \mathcal{L}\sigma_{ij}^M = \sigma_{ij}^M + \lambda \frac{\partial \sigma_{ij}^M}{\partial t},$$

and hence

$$P - P^M = \int_S u_i (\sigma_{ij} - \sigma_{ij}^M) n_j dS = \int_S u_i \lambda \frac{\partial \sigma_{ij}^M}{\partial t} n_j dS.$$

However, as we have seen from Figs. 1b, 2a and 2d, there is a single dominant angular frequency ω, such that

$$\frac{\partial}{\partial t} \sim \omega$$

and the Deborah number is given by $De = \lambda \omega \approx 0.2$. Hence the scale of the relative error in using the Newtonian power, P, to approximate the linear Maxwell power, P^M, is given by

$$\left| \frac{P - P^M}{P^M} \right| \sim O\left(\frac{\int_S u_i \lambda \omega \sigma_{ij}^M n_j dS}{\int_S u_i \sigma_{ij}^M n_j dS} \right) \sim O(De),$$

and thus the relative error is of the scale of the Deborah number, as used and stated in the main text.

Supplementary material

Supplementary material associated with this article can be found, in the online version, at doi:10.1016/j.jtbi.2018.02.013.

References

Bale, R., Hao, M., Bhalla, A.P.A., Patankar, N.A., 2014. Energy efficiency and allometry of movement of swimming and flying animals. Proc. Nat. Acad. Sci. 111 (21), 7517–7521.

Brokaw, C.J., 1966. Effects of increased viscosity on the movements of some invertebrate spermatozoa. J. Exp. Biol. 45, 113–139.

Brokaw, C.J., 1971. Bend propagation by a sliding filament model for flagella. J. Exp. Biol. 55, 289–304.

Camalet, S., Jülicher, F., 2000. Generic aspects of axonemal beating. New J. Phys. 2, 24.1–24.2.

Cortez, R., 2001. The method of regularized stokeslets. SIAM J. Sci. Comput. 23, 1204–1225.

Khan, M.A., Litt, M., Wolf, D.P., Blasco L, L., 1977. Human cervical-mucus. II. Changes in viscoelasticity during the menstrual cycle. Fertil. Steril. 28, 47–52.

Dresdner, R., Katz, D., 1981. Relationship of mammalian sperm motility and morphology to hydrodynamic aspects of cell function. Biol. Reprod 25, 920–930.

Fawcett, D.W., 1975. The mammalian sperm. Dev. Biol. 44, 394–436.

Gaffney, E.A., Gadêlha, H., Smith, D.J., Blake, J.R., Kirkman-Brown, J.C., 2011. Mammalian sperm motility: observation and theory. Annu. Rev. Fluid Mech. 43, 501–528.

Gray, J., Hancock, G.J., 1955. The propulsion of sea urchin spermatozoa. J. Exp. Biol. 32, 802–814.

Hilfinger, A., Chattopadhyay, A.K., Jülicher, F., 2009. Nonlinear dynamics of cilia and flagella. Phys. Rev. E 79, 051918.

Ishimoto, K., Gadêlha, H., Gaffney, E.A., Smith, D.J., Kirkman-Brown, J., 2017. Coarse–graining the fluid flow around a human sperm. Phy. Rev. Lett. 118, 124501.

Ishimoto, K., Gaffney, E.A., 2014. A study of spermatozoan swimming stability near a surface. J. Theor. Biol. 360, 187–199.

Ishimoto, K., Gaffney, E.A., 2016. Mechanical tuning of mammalian sperm behaviour by hyperactivation, rheology and substrate adhesion: a numerical exploration. J. R. Soc. Interface 13, 20160633.

Ishimoto, K., Gaffney, E.A., 2017. Boundary element methods for particles and microswimmers in a linear viscoelastic fluid. J. Fluid Mech. 831, 228–251.

Jülicher, F., Prost, J., 1997. Spontaneous oscillations of collective molecular motors. Phys. Rev. Lett. 78, 4510–4513.

Kirkman-Brown, J.C., Smith, D.J., 2011. Sperm motility: is viscosity fundamental to progress? Mol. Hum. Reprod. 17, 539–544.

Kralemann, B., Cimponeriu, L., Rosenblum, M., Pikovsky, A., Mrowka, R., 2008. Phase dynamics of coupled oscillators reconstructed from data. Phys. Rev. E 77, 066205.

Lindemann, C.B., 1994a. A geometric clutch hypothesis to explain oscillations of the axoneme of cilia and flagella. J. Theor. Biol. 168, 175–189.

Lindemann, C.B., 1994b. A model of flagellar and ciliary functioning which uses the forces transverse to the axoneme as the regulator of dynein activation. Cell Motil. Cytoskelton 29, 141–154.

Lindemann, C.B., 1996. Functional significance of the outer dense fibers of mammalian sperm examined by computer simulations with the geometric clutch model. Cell Motil. Cytoskelton 34, 258–270.

Lindemann, C.B., Leisch, K.A., 2010. Flagellar and ciliary beating: the proven and the possible. J. Cell Sci. 123, 519–528.

Lindemann, C.B., Mitchell, D.R., 2007. Evidence for axonemal distortion during the flagellar beat of chlamydomonas. Cell Motil. Cytoskel. 64, 580–589.

Lopez-Garcia, M.D.C., Monson, R.L., Haubert, K., Wheeler, M.B., Beebe, D.J., 2008. Sperm motion in a microfluidic fertilization device. Biomed. Microdevices 10, 709–718.

Ma, R., Klindt, G., Riedel-Kruse, I., Jülicher, F., Friedrich, B., 2014. Active phase and amplitude fluctuations of flagellar beating. Phys. Rev. Lett. 113, 048101.

Oiwa, K., Takahashi, K., 1988. The force-velocity relationship for microtubule sliding in demembranated sperm flagella of the sea urchin. Cell Struct. Funct. 13, 193–205.

Oriola, D., Gadêlha, H., Casademunt, J., 2017. Nonlinear amplitude dynamics in flagellar beating. R. Soc. Open Sci. 4 (3), 160698.

Pozrikidis, C., 1992. Boundary Integral and Singularity Methods for Linearized Viscous Flow. Cambridge University Press.

Riedel-Kruse, I.H., Hilfinger, A., Howard, J., Jülicher, F., 2007. How molecular motors shape the flagellar beat. HFSP J 1, 192–208.

Rikmenspoel, R., 1984. Movements and active moments of bull sperm flagella as a function of temperature and viscosity. J. Exp. Biol. 108, 205–230.

Seo, D., Agca, Y., Feng, Z.C., Critser, J.K., 2007. Development of sorting, aligning, and orienting motile sperm using microfluidic device operated by hydrostatic pressure. Microfluid. Nanofluid. 3, 561–570.

Shao, B., Shi, L.Z., Nascimento, J.M., Botvinick, E.L., Ozkan, M., Berns, M.W., Esener, S.C., 2007. High-throughput sorting and analysis of human sperm with a ring-shaped laser trap. Microfluid. Nanofluid. 3, 561–570.

Shum, H., Gaffney, E.A., Smith, D.J., 2010. Modelling bacteria behaviour close to a no-slip plane boundary: the influence of bacterial geometry. Proc. R. Soc. Lond. A 466, 1725–1748.

Smith, D.J., Blake, J.R., 2009. Surface accumulation of spermatozoa: a fluid dynamic phenomenon. Math. Sci. 34, 74–87.

Smith, D.J., Gaffney, E.A., Blake, J.R., Kirkman-Brown, J.C., 2009a. Human sperm accumulation near surfaces: a simulation study. J. Fluid Mech. 621, 289–320.

Smith, D.J., Gaffney, E.A., Gadêlha, H., Kapur, N., Kirkman-Brown, J., 2009b. Bend propagation in the flagella of migrating human sperm, and its modulation by viscosity. Cell Motil. Cytoskeleton 66, 220–236.

Suarez, S.S., Pacey, A.A., 2006. Sperm transport in the female reproductive tract. Hum. Reprod. Update 12, 23–37.

Wakeley, P. W., 2008. Optimisation and Properties of Gamete Transport. Ph. D. Thesis, University of Birmingham, UK, http://etheses.bham.ac.uk/4944/.

Werner, S., Rink, J.C., Riedel-Kruse, I.H., Friedrich, B.M., 2014. Shape mode analysis exposes movement patterns in biology: flagella and flatworms as case studies. PLoS ONE 9 (11), e113083.

Woolley, D.M., 2003. Motility of spermatozoa at surfaces. Reproduction 126, 259–270.